Enhanced bond switching at complexion layer facilitates high fracture energy of LATP solid-state electrolytes

Chen, Zhimin; Du, Tao; Krishnan, N. M. Anoop; Smedskjær, Morten Mattrup

Published in:
Journal of Materials Chemistry A

DOI (link to publication from Publisher):
10.1039/D3TA05122F

Publication date:
2024

Document Version
Accepted author manuscript, peer reviewed version

Enhanced bond switching at complexion layer facilitates high fracture energy of LATP solid-state electrolytes

Zhimin Chen[1], Tao Du[1], N. M. Anoop Krishnan[2], Morten M. Smedskjaer[1,*]

[1] *Department of Chemistry and Bioscience, Aalborg University, Aalborg East 9220, Denmark*

[2] *Department of Civil Engineering, Indian Institute of Technology Delhi, Hauz Khas, New Delhi 110016, India*

** Corresponding author. E-mail: mos@bio.aau.dk*

Abstract

Understanding the mechanical behavior of solid-state electrolytes is pivotal for the development of all-solid-state batteries. Using large-scale molecular dynamics simulations, here we show that $Li_{1.3}Al_{0.3}Ti_{1.7}(PO_4)_3$ (LATP) glass-ceramics, a promising solid-state electrolyte, feature an enhanced bond switching at the complexed glass-crystal interface, thereby facilitating their high fracture energy. Specifically, we study the mechanical behavior of LATP during tensile simulations, focusing on the crack propagation. We find that the fracture behavior is strongly influenced by the size of the nanograins and their positions relative to the pre-crack, and the complexed interface is found to be susceptible to concentrated shear deformation. The fracture energy of LATP glass-ceramics is enhanced for larger grains, since these have higher contact area with the glass phase and thus a larger complexed interface. Based on structural analyses during the tensile process, we demonstrate the occurrence of enhanced bond switching events at complex interfaces. These events dissipate the strain energy associated with the fracture process. Particularly in cases where cracks tend to propagate along the interfaces, this enhancement significantly improves the fracture energy of LATP glass-ceramic electrolytes.

1. Introduction

The performance of lithium-ion batteries (LIBs) has improved since their discovery and they are now widely used in portable energy storage devices, electric vehicles, etc.[1–3] Conventional LIBs use an organic liquid electrolyte, which suffers a risk of combustion and leakage and thus challenges the safety of the battery. The energy and power density of conventional LIBs are also relatively low, making it difficult to meet the future demand for safe, yet high-performance batteries.[4–6] All solid-state batteries (ASSBs) with solid-state electrolytes (SSEs) are considered as one of the most promising next-generation energy storage devices,[7] due to their high safety[5,8], thermal stability and chemical resistance. In addition, SSEs with high ionic conductivity can ensure improved power density and charge/discharge rates,[9] as well as higher energy density and longer cycle life compared to liquid electrolytes.[10] SSEs are classified according to their structure and composition, with inorganic solid electrolytes (e.g., oxides, phosphates, etc.) having high ionic conductivity and chemical stability, but suffer from lower mechanical flexibility and processing difficulties. Organic solid electrolytes (e.g., polymers) have high mechanical strength and flexibility, but relatively low ionic conductivity.[5]

A promising SSE material is $Li_{1+x}Al_xTi_{2-x}(PO_4)_3$ (LATP) glass-ceramic (i.e., a composite multiphase material containing crystals embedded in a glassy matrix) due to its excellent room-temperature ionic conductivity (10^{-4} to 10^{-3} S cm^{-1})[11,12] and chemical and thermal stability.[11] However, ASSBs assembled with oxide SSEs such as LATP are subject to mechanical deformation and stress concentration during cycling (due to volume changes in the electrodes), which can result in cracking and thus decline in battery performance.[13] Consequently, the mechanical properties of SSEs, including stiffness, crack initiation resistance, and fracture toughness, need to be understood and improved to design high-performance ASSBs.[6,13] In particular, this is needed to significantly enhance the stability, safety, and cycling capability of batteries, but these mechanical properties remain relatively poorly studied so far.[14–17] Beyond the bulk mechanics, the mechanical performance of interfacial layers play an important role in ASSBs. The most studied interface so far is the solid electrolyte interphase (SEI) layer, as the mechanical integrity of this layer determines the longevity and efficiency of the battery.[18] Crack formation and propagation within the SEI directly impact lithium consumption, electrolyte drying, heightened impedance, and dendrite growth.[18] These factors ultimately result in diminished capacity and premature failure of the battery.[18] In addition to the SEI, the presence of nano-sized interphases, such as those between grains in ceramics,[19] which are termed complexions as they are thermodynamically stable state and physically distinct from the abutting bulk phases,[20,21] also need to be considered. Such stable interfaces in glass-ceramic electrolytes can be also termed complexions in the case of the amorphous phases complexing with grains.[21] However, the mechanical behavior of these interfaces in such LATP glass-ceramics is not well understood.

The bulk LATP glass-ceramics prepared throughout heat-treatment of the precursor bulk LATP glass exhibit higher ionic conductivity (~ 1×10^{-4} S cm^{-1}, much higher than the value of 6×10^{-5} S cm^{-1} for LATP ceramic and 10^{-10}-10^{-8} S cm^{-1} for LATP glass[22]) compared to those prepared through other methods, such as sol-gel, and solid state methods.[11,23] For example, synthesis of LATP ceramics through conventional powder-sintered routes can result in a limited number of pores, which is detrimental to the overall conductivity of ASSBs.[24] By using the melt-quenching technique to make the precursor glass, these voids can be eliminated and the material can be easily shaped into the desired form. Subsequently, the crystalline morphology of the glass-ceramic products can be

controlled based on the heat-treatment protocol.[23] For example, the ionic conductivity of LATP glass-ceramics can be improved in this way[23,25–27] but there are few comprehensive studies on their mechanical properties. This hinders our understanding of the fracture behavior of LATP electrolytes.

In this study, we use large-scale molecular dynamics (MD) simulations to gain an in-depth understanding of the mechanical properties of LATP glass-ceramics at the atomic scale. Simulations are needed since experimental mapping of the atomic structure of disordered materials under an applied stress remains to be highly challenging, if not impossible. We here study the composition of $Li_{1+x}Al_xTi_{2-x}(PO_4)_3$ for x=0.3, as it has the highest ionic conductivity among different LATP derivatives.[24] To enable fracture simulations, we are using a classical force field that has been developed recently for $Li_{1.3}Al_{0.3}Ti_{1.7}(PO_4)_3$.[21] This specifically parameterized force field has been found to more accurately represent $Li_{1.3}Al_{0.3}Ti_{1.7}(PO_4)_3$ at high temperature (which is important for the melt-quenching process to form glass phases) as compared to the ready-to-use ReaxFF force field[28]. We prepare the LATP glass-ceramics using the cut-and-combine method[29,30] and then perform systematic tensile simulations on various LATP microstructures, including crystal volume fraction, length to diameter (*L*/*D*) ratio, etc.. Finally, we correlate the fracture behavior with analyses of bond switching events,[31] which originate from bond breaking and re-formation during the tensile strain process.[32,33] We demonstrate that LATP exhibits high fracture energy due to enhanced bond switching events at the complexed interface between crystalline and glass phases in the LATP glass-ceramic electrolytes.

2. Results and Discussion

Structure of glasses, crystals, and glass-ceramics. To model the glass-ceramic structure, we start with the crystal $LiTi_2(PO_4)_3$ (LTP), as shown in **Figure 1a**. Based on the modification of the LTP structure, the crystalline phase of LATP glass-ceramics can be obtained by partial substitution of Ti by Al in the LTP crystalline phase[11,12,34]. The modeled crystalline phase of $Li_{1.3}Al_{0.3}Ti_{1.7}(PO_4)_3$ has been confirmed as the phase also obtained through crystallization from the experimental LATP glass, as outlined in the **Methods** section for experimental details. In the following, we therefore investigate the electrolyte with composition of $Li_{1.3}Al_{0.3}Ti_{1.7}(PO_4)_3$. To this end, we first transferred the initial trigonal LTP to an orthogonal cell. Then, we partially replaced Ti^{4+} in LTP with Al^{3+} with charge neutrality maintained by introducing an excess amount of Li^+ at the thermodynamically more stable M_2 site.[28,35] The glassy state of the LATP was produced through conventional melt-quenching using MD simulation; the detailed procedure can be found in the **Methods** section.

The density of LATP crystal and LATP glass obtained from MD simulation are 2.84 and 2.64 $g.cm^{-3}$, respectively, which are in good agreement with experimental values of 2.84 and 2.69 $g.cm^{-3}$, respectively, as measured by Archimedes method.[36,37] The structural details of the LATP glassy state are also in excellent agreement with *ab initio* molecular dynamics (AIMD) simulations results as presented in **Figure S1** and **Figure S2**. A snapshot of a simulated LATP glass sample, showing the location of the different atoms, is presented in **Figure 1b**, differing from the crystalline LATP structure which only contains Al-O octahedra, whereas the glass structure contains both four- and five-fold coordinated Al. As shown in **Figure S3a**, we also observe some six-fold coordinated Al in the glass. The structure snapshots are shown in **Figure 1c** (partial enlargement of **Figure 1b**). The coordination number (CN) of Ti in the LATP glass is mainly 6, and less than 30% five-fold coordinated Ti (**Figure S3b**). For these simulations, we use a box dimension of 34.08 Å × 486.93 Å

× 333.41 Å with a composition of $Li_{1.3}Al_{0.3}Ti_{1.7}(PO_4)_3$ for both crystal and glass phases, and the glass-ceramic electrolytes are then prepared by the cut-and-combine method,[29] that is, by cutting the crystal (as inclusion) and glass (as matrix) to a complementary structure, and combining them afterward. A subsequence annealing process is done to heal the fresh contact surface.

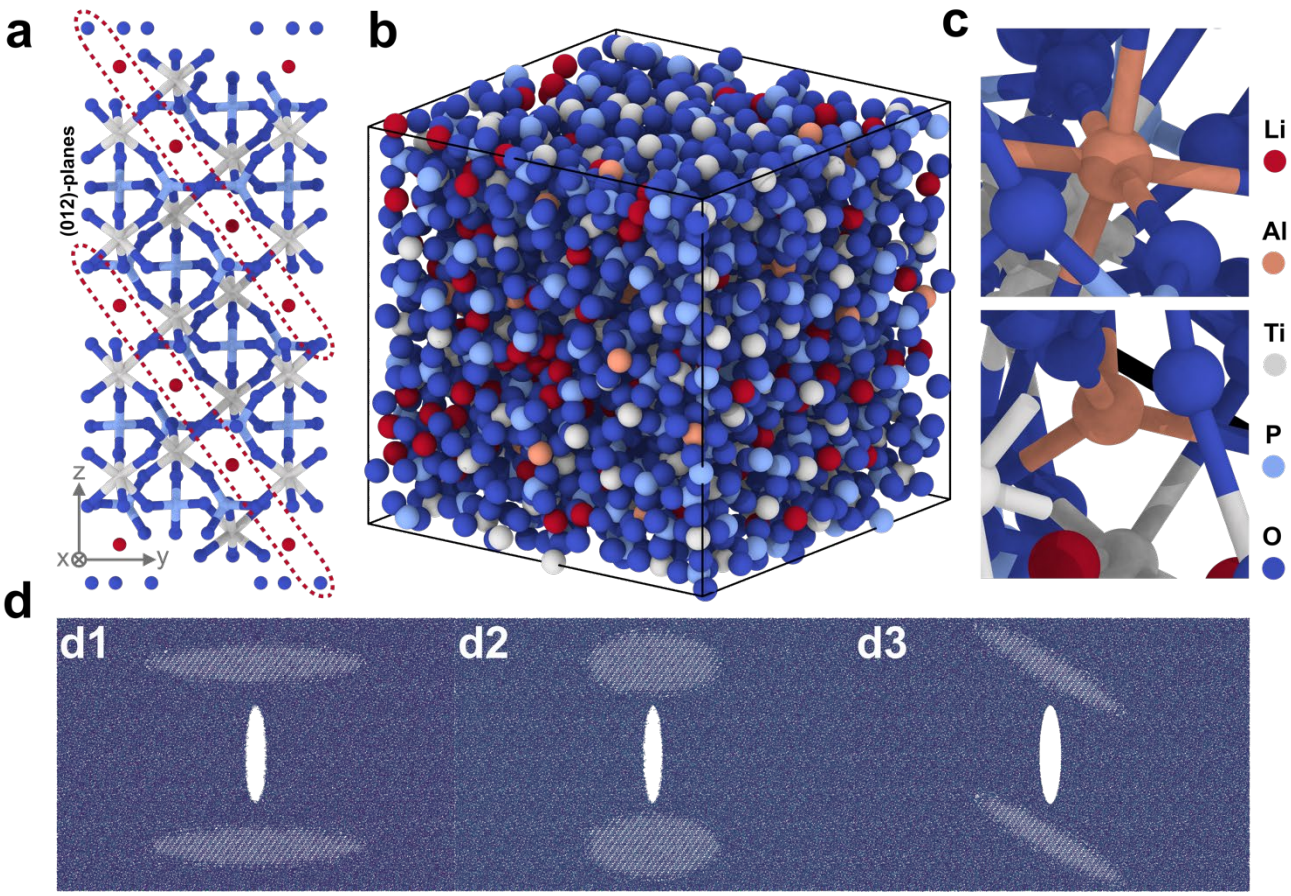

Figure 1. Structure information of simulated LATP electrolytes. (a) Atomic structure of the redefined orthogonal cell of $LiTi_2(PO_4)_3$ crystal. (b) Atomic snapshot of the simulated LATP glass, highlighting the presence of both (c) 6-fold (top panel) and 4-fold (bottom panel) coordinated Al units. (d) Atomic snapshots of LATP glass-ceramics with induced pre-cracks. (Left) d1 LATP-GC15 sample with fixed *L*/*D* ratio equal to 5/1 of nanograins. (Middle) d2 is an example of LATP-GC15 with nanograins of *L*/*D* equal to 2/1. (Right) d3 shows LATP-GC3 and the angle between the nanograins and pre-crack (white ellipse) is 60º.

The two-dimensional (2D) slab model of LATP glass-ceramics is then constructed as exemplified in **Figure 1d**, with the white ellipse representing the pre-crack that is introduced for the fracture simulation (as described below). The factors considered for investigating the mechanical properties of LATP electrolytes include the inserted size of grains, the *L*/*D* ratio of the grain, and the angle between the grain and the pre-crack. Atomic snapshots for some of these structures are presented in **Figure 1d**. The crystal volume content in the glass-ceramic is highlighted in the samples' IDs, e.g., LATP-G represents the glass sample, LATP-C represents the crystalline sample (i.e., the bulk LATP samples that is fully crystalline), and LATP-GC15 represents that the LATP crystal in the LATP glass-ceramic accounts for 15 vol%. The detailed information of the investigated samples is provided in

Table S1.

We first analyze the cation coordination environments in the glass, crystal, and glass-ceramic phases of LATP based on the radial distribution functions (RDFs) at 300 K. The left hand-side panels of **Figure 2** present the RDFs for Al-O and Ti-O, which those of the other pairs are presented in **Figure S4**. A smaller Al-O pair distance is observed in the glass-matrix sample (i.e., in LATP glass and glass-ceramic) compared to that in crystalline LATP, whereas the same decrease is not found for the Ti-O pair upon vitrification. This can be attributed to the decrease of Al CN as observed in the $n(r)$ in **Figure 2** (right panel), i.e., these integrated RDFs provide the local coordination information. The Ti-O pair features a similar coordination environment in glass and crystal phases, with a dominance of 6-fold coordination. In LATP glasses and glass-ceramics, an average CN of 5 for Al-O is observed. The bond angle distributions in the insets of **Figure 2** show that the O-Al-O and O-Ti-O angles are centered at approximately 90º, with an additional peak below 180º ascribed to the diagonal angles of the Al-O and Ti-O octahedra.

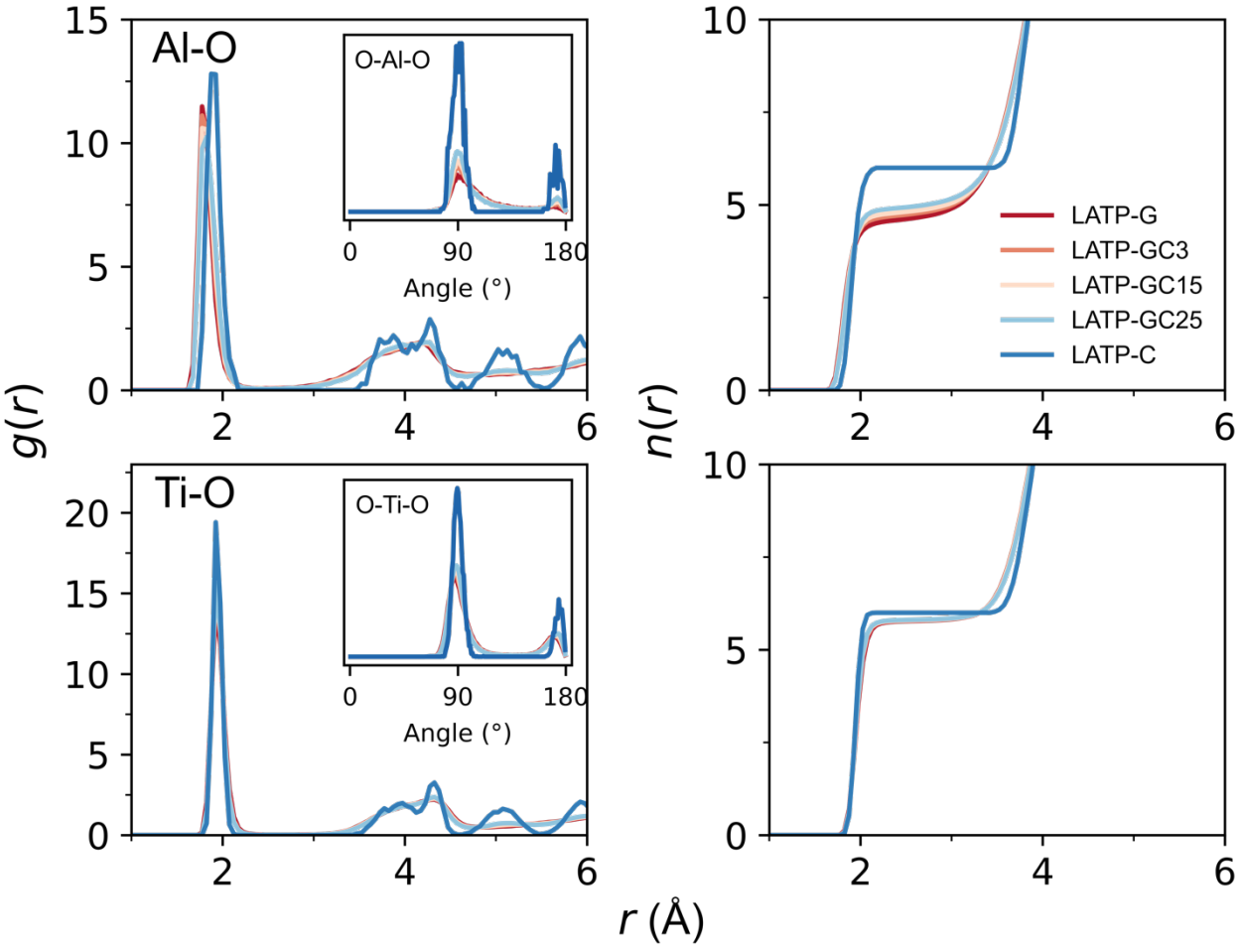

Figure 2. Radial distribution functions $g(r)$ and integrations $n(r)$ of Al-O (upper panels) and Ti-O pairs (lower panels) for LATP glass, glass-ceramics, and crystal at 300 K. Insets: angular distribution functions of O-Al-O and O-Ti-O.

Fracture behavior. As described above, we introduce an elliptical pre-crack into the constructed

atomic structure of the LATP glass-ceramics and investigate the mechanical behavior during tensile simulations. Details of the fracture simulations are described in the Methods section. Although the failure behavior of LATP electrolytes in solid-state batteries is influenced by several factors, such as the mechanical evolution of SEI, stress/strain generated in the cell, and the volume change of electrode etc.,[6,14,15,38] the intrinsic mechanical properties of LATP are fundamental to understanding crack formation, propagation, and fracture behavior in solid electrolytes. Typically, elastic modulus and fracture toughness are considered among the most important indicators of battery performance.[6]

The top panel of **Figure 3a** shows the stress-strain curves during uniaxial tensile processes for different sizes of nanograins in the LATP glass-ceramics, where the orientation of the crystals in the LATP-C sample is consistent with the orientation of the nanograins in the glass-ceramic. We find that the LATP crystal's mechanical properties are influenced by its orientation. For instance, as depicted in **Figure S5**, a 90-degree rotation leads to a reduction in the crystal's modulus (slope of stress-strain curve before strain equal 0.01) and a decrease in fracture energy (area of stress-strain curve). In the following, we have selected the orientation characterized by a higher modulus (the orientation as presented in **Figure 1a**). Based on the stress-strain curves, the Young's modulus, as reflected by the slope in this region, is found to increase with the increase in the crystal content (larger nanograins) in the glass-ceramics. The simulated modulus of the LATP crystal for this crystal orientation is 139.1 GPa (bottom panel of **Figure 3a**), which is comparable to that from experiments and first principle calculations (107-150 GPa).[39,40] Overall, the LATP samples exhibit brittle fracture, with rapid complete fracture after crack propagation begins, but the glass-ceramics with larger nanograins possess better resistance to crack propagation, i.e., higher fracture energy, as shown in the bottom panel of **Figure 3a**. It is important to note that, although LATP glass-ceramics exhibit improved Young's modulus compared to the precursor glass, they still fall short of the Young's modulus of the crystals. This limitation arises from the relatively low crystallinity of the constructed glass-ceramics, with a maximum volume fraction of 25% crystals. To provide clarity, we developed a crystalline LATP model, denoted as LATP-GC85 (with crystal content of 85 vol%), utilizing the LATP crystalline phase as a matrix. The Young's modulus and stress-strain curves of this LATP glass-ceramic electrolyte, achieved by increasing the crystal content, closely align with those exhibited by the LATP crystal (**Figure S6**). On the other hand, we note that the glass-ceramics show improved fracture energy compared to both the pure glass and crystal phases.

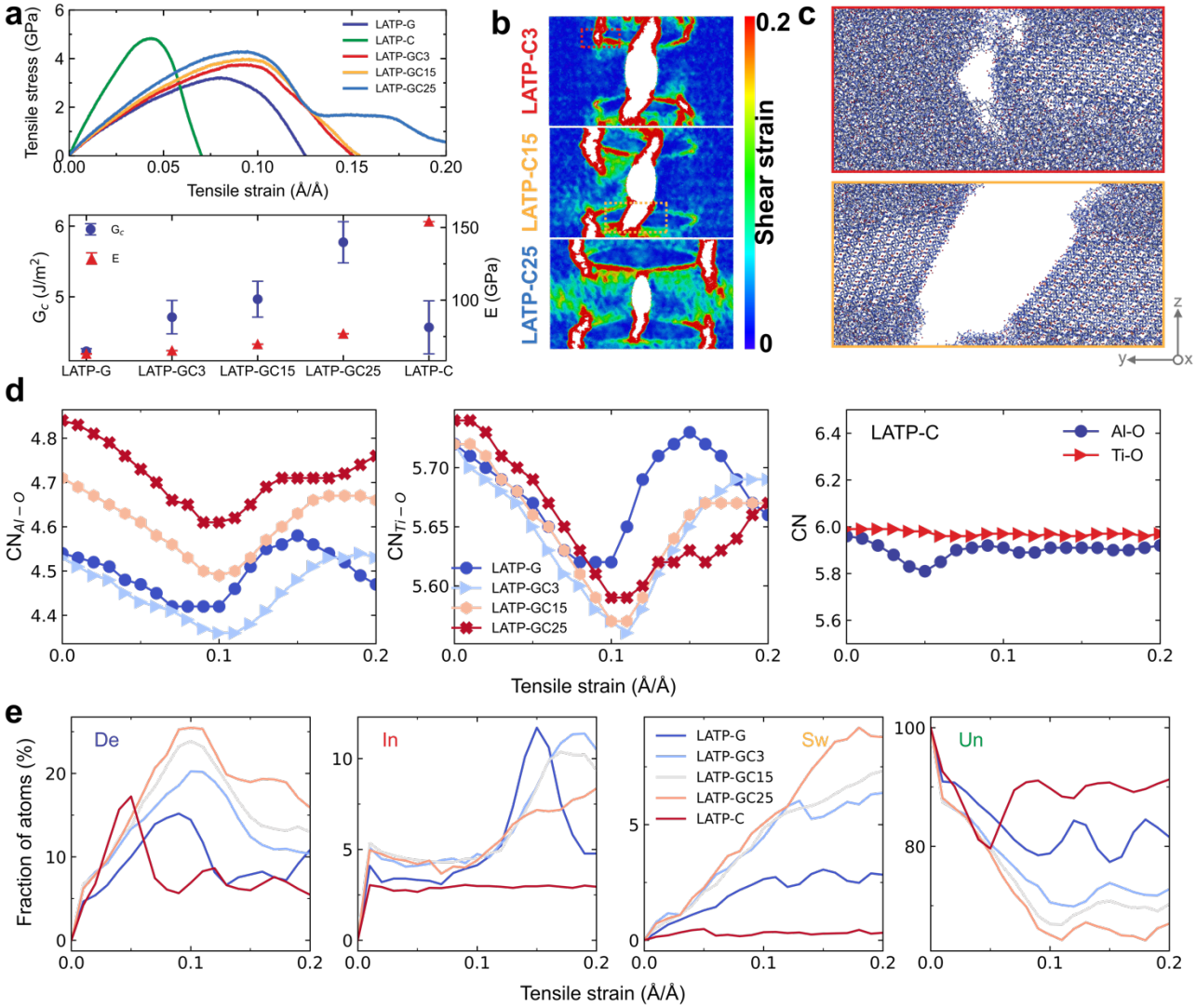

Figure 3. Fracture behavior of LATP electrolytes. (a) Strain-stress curves during the uniaxial tensile process (top) and resulting values of fracture energy G_c and Young's modulus E (bottom) for the different samples. The orientation of crystal inserted in the LATP glass-ceramics is set to be the same as that in the LATP-C sample. (b) Distribution of shear strain in LATP glass-ceramics at strain of 0.15. The atoms are color coded by current shear strain values compared to that in the non-strained configuration. (c) Atomic snapshots of microcrack and cleavage fracture for LATP-GC3 (top) and LATP-GC15 (bottom) electrolytes at strain of 0.15. (d) Coordination number (CN) changes for Al-O and Ti-O in LATP electrolytes during tensile process. The left and center panels show results for LATP glass and glass-ceramics, while the right panel shows results for the LATP crystal. (e) Fraction of bond switching events for Al-O as a function of the tensile strain, including decreased CN (De), increased CN (In), swapped CN (Sw), and unchanged CN (Un).

As shown in **Figure 3b**, the shear deformation is concentrated at the interface between the nanograins and the glass matrix (i.e., so-called complexion layer), and thus not only in the vicinity of the crack. By tracing the structural changes during the fracture process, it is evident that interfacial bonds are broken and microcracks appear. In addition, the propagating cracks do not bypass all crystals and the nanograins extend the crack path at the cleavage surface, i.e., cleavage fracture, as

shown in **Figure 3c**. Next, we consider the tensile simulations for different nanograin shapes (length-to-diameter *L*/*D* ratios) and angles relative to the pre-crack in the glass-ceramics. The atomic snapshots and stress-strain curves for these glass-ceramics are shown in **Figure S7a-c** and **Figure S7d-e**, respectively. Glass-ceramics with the same crystal volume fraction but varying *L/D* ratio of nanograins exhibit different fracture behaviors. That is, for a larger *L*/*D* ratio, a larger stress is needed to induce crack propagation (**Figure S7d**). This is because the crack is prone to propagate along the interface as shown in **Figure S7a** and increased *L/D* ratio results in a larger contact area, i.e., complexed interface. However, the cracks tend to propagate through the nanograins in the glass-ceramics with elongated grains (i.e., when *L*/*D* ratio increases from 2/1 and 3/1 to 4/1 and 5/1) as presented in **Figure S7c**. This also allows for higher stress resistance before fracture occurs compared to scenarios where the crack bypasses the nanograins. The location of the nanograins in the structure also affects the crack propagation paths, as shown in **Figure S7e**. That is, the larger the angle between the nanograins and the pre-crack (i.e., the closer the crack tip and the complexed interface are to a straight line), the easier it is for the crack to propagate along the interface until fracture.

We next analyze the breakage and reformation of bonds during the tensile processes. **Figure 3d** shows the change in the total CNs of Al and Ti during the tensile process. The results for P-O pairs are not shown, since no changes in the P CN occurs. In the glass and glass-ceramics, the CNs of Al-O and Ti-O decrease with strain, reaching a minimum at the point of fracture initiation (strain ~ 0.1) as bond breakage dominates for strain values from 0 to 0.1 (see left and center panels in **Figure 3d**). The LATP-G sample is fully fractured at strain ~0.15 and the CN changes afterwards due to the relaxation of the fractured structure. In contrast, during the process of rapid crack propagation and fracture, the CNs increase as new fracture surface formation is accompanied by bond reformation until the system is completely fractured at a strain above ~0.15. We thus observe changes in the CNs of Al-O and Ti-O for both glass and glass-ceramic systems, but for the LATP crystals, only the Al CN is found to drop to a minimum at the onset of fracture, whereas the Ti CN is relatively constant with strain (see right panel in **Figure 3d**).

The bond switching activities cannot be determined from the average CN evolutions, so we also calculate the coordination environment of each atom relative to that in their non-strained state,[31,32] including decreasing CN (De), increasing CN (In), swapped CN (Sw), and unchanged CN (Un) as shown schematically in **Figure S8**. The fraction of these bond switching events as a function of strain for Al-O are presented in **Figure 3e**. Collectively, more bond switching events occur for larger nanograins in LATP, with LATP-GC25 exhibiting the most bond switching activities. Bond swapping events in glass and glass-ceramics continue to increase throughout the tensile process. This is not observed in LATP crystals, and the In-events are also almost absent in LATP crystals, i.e., De-events dominate. The bond switching events for Ti-O show similar trends as those for Al-O (**Figure S9**). The increased crystal content in the glass-ceramics leads to the increasing of bond switching events, and the same is reflected in the decreasing fraction of Un events. That is, although we find relatively few bond switching activities in the crystalline phase for LATP-C from **Figure 3e**, the partially crystalline glass-ceramics (LATP-GC3, LATP-GC15, and LATP-GC25) exhibit higher bond switching activity (and higher fracture energy, **Figure 3a**) with increasing crystalline phase content.

Enhanced bond switching activities in complexion layer. To further analyze the trends in bond switching described above, we study the complexed interface of LATP-GC15 with a thickness of 1

nm. As reported in the literature, the width of a complex interface can be quantitatively characterized by the two-dimensional Fourier transform of the simulated system, which is approximately 1.45 nm.[21] In this work, we quantify the bond-switching events in the interface by varying the width of the complex interface. As shown in **Figure S10**, the Un events that increase at a width of 1 nm are defined as the interface. Further increasing the width (within a reasonable range, i.e., not extending excessively into the glass matrix) does not significantly affect the bond-switching events counted at the interface h. The fraction of unchanged bond activities (Un events) occurring at the interface is found to be lower than that of the glass, crystal, and glass-ceramic systems (**Figure 4a**). Namely, bond switching is enhanced at the interface. As the size of the nanograins in glass-ceramics increases, there is a larger contact area between nanograins and glass matrix, creating a larger complexed interface, as illustrated in **Figure S11**. This is evident from the enhanced bond switching events for glass-ceramics with larger grains (**Figure 3e**). As bond switching events can dissipate strain energy during fracture process,[32,33] the enhanced bond switching events at the complexed interface noticeably improves the fracture energy of the LATP glass-ceramics (**Figure 3a**) as compared to LATP glasses where cracks have a propensity to propagate along the interfaces (**Figure 3b**).

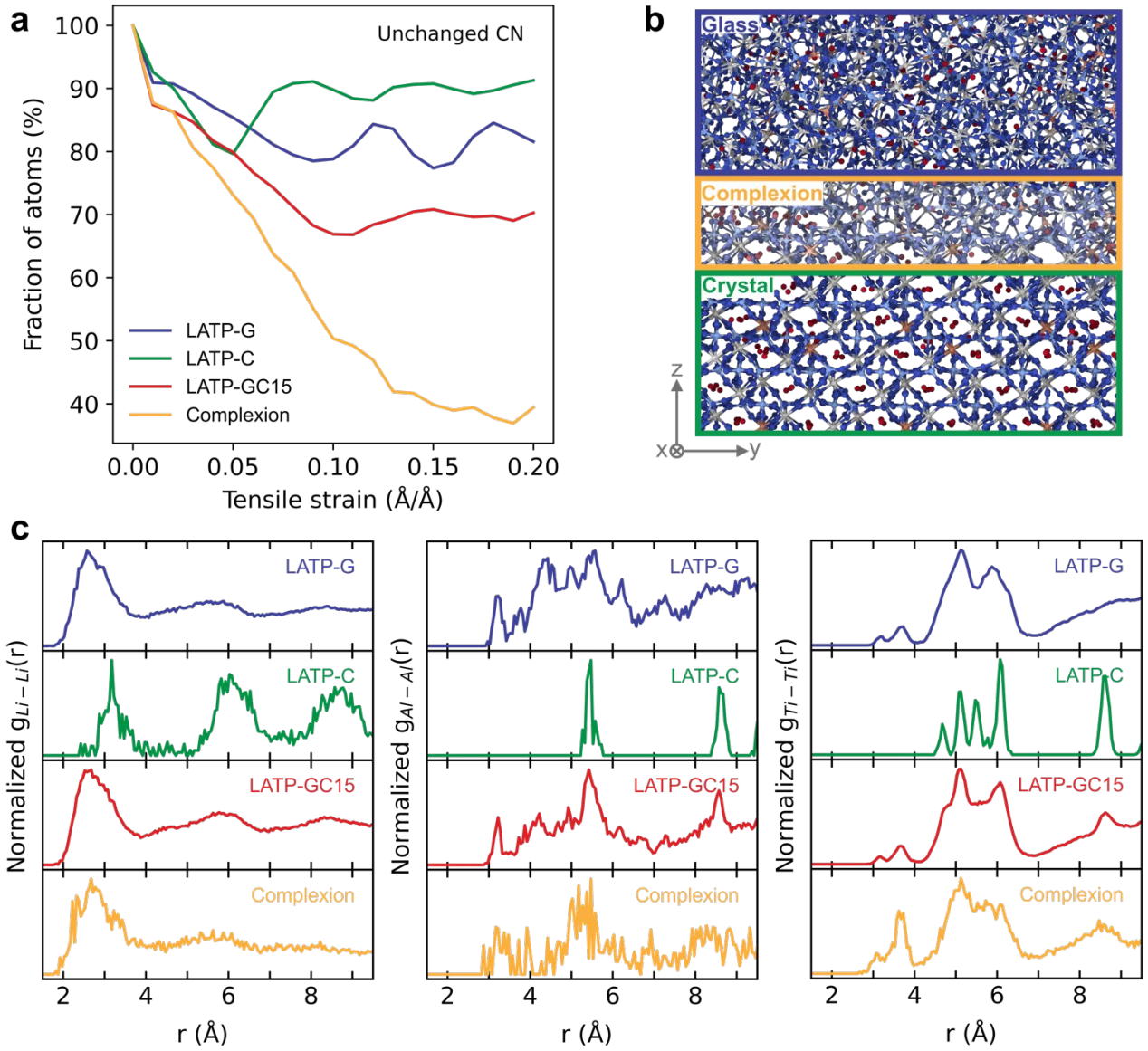

Figure 4. Bond switching activities at the complexion interface of LATP glass-ceramic electrolytes. (a) Fraction of unchanged CN events as function of tensile strain. (b) Atomic snapshot of complexion in LATP-GC15 glass-ceramic. (c) Normalized partial radial distribution functions of Li-Li (left), Al-Al (center), and Ti-Ti (right) pairs in LATP electrolytes.

The structure network of the defined complexion layer is obviously distinct from the glass and crystalline phases as shown in **Figure 4b**, which is an extracted partially-complexed interface of LATP-GC15. We further consider the structural distinctions between the complexed interface, the glass phase, the crystalline phase, and the glass-ceramic phase based on the Li-Li, Al-Al, and Ti-Ti RDFs in **Figure 4c**. We find that the cation distances in the complexed interface layer exhibit similarities to those in the glass phase, and the broadened distribution of cations enables a looser and more flexible structural network. This likely increases the propensity for bond switching events in the complexion layer relative to that in the crystalline phases with ordered crystal structure.

3. Conclusions

LATP is one of the most promising solid-state electrolyte systems, and despite its many advantages such as high room temperature ionic conductivity and chemical stability, its intrinsic mechanical properties need to be understood before scale-up. Here, we investigated the fracture behavior at the atomic level using large-scale MD simulations. The results show that large grains in LATP provide higher fracture energy, and that the appearance of microcracks and the crack propagation occur at the interface due to the concentration of shear strain at the crystal-glass phase interface. Consequently, the shape of the grains and the angle of the grain position relative to the pre-crack are important factors affecting the fracture energy. During the fracture process of LATP glass-ceramics, the breaking and reforming of Al-O and Ti-O bonds in the glass phase are the main energy dissipating processes, while the more stable Ti-O bonds in the crystal phase has no bond switching behavior throughout the tensile process. The overall bonding activity shows a decrease in the Al-O coordination number. Finally, we find the increased fracture energy can be attributed to the enhanced bond switching events at the interface, as the bond switching events provide the ability of dissipating fracture energy.

4. Methods

Experimental synthesis of LATP samples. Glassy electrolyte with molar composition of $Li_{1.3}Al_{0.3}Ti_{1.7}(PO_4)_3$ was synthesized by the melt-quenching method. Lithium carbonate (Li_2CO_3, ≥98.5%, Merck KGaA), aluminum oxide (Al_2O_3, ≥99.5%, Merck KgaA), titanium dioxide (TiO_2, ≥99.5%, Merck KgaA), and ammonium dihydrogen phosphate ($NH_4H_2PO_4$, ≥99.5%, Merck KgaA) were used as raw materials for preparing the glasses. Raw materials were melted in an Al_2O_3 crucible at ~1450 °C for ~2 h and then quenched onto a brass plate. The samples were annealed at their glass transition temperature (T_g), determined by differential scanning calorimetry (DSC, STA 449 F3 Jupiter, Netzsch), for 30 min. Samples were also heat-treated at 950 °C for 1 h to obtain glass-ceramics. Subsequent powder X-ray diffraction (Empyrean XRD, PANalytical) analysis confirmed the non-crystalline nature of the LATP glass and the crystalline diffraction peaks of the LATP glass-ceramic (**Figure S12**).

Molecular dynamics simulations. Molecular dynamics (MD) simulations were performed using the Large-scale Atomic/Molecular Massively Parallel Simulator (LAMMPS) software package.[41] Atomic structure was visualized by Ovito.[42] We used a combination of long-range Coulomb interactions and short-range Buckingham terms to express the interatomic interactions (**Eq.1**), [21]

$$U_{ij} = \frac{1}{4\pi\epsilon_0}\frac{q_i q_j}{r_{ij}} + A_{ij}\exp\left(-\frac{r_{ij}}{\rho_{ij}}\right) - \frac{C_{ij}}{r_{ij}^6}. \quad (1)$$

Specifically, a core-shell model implemented in LAMMPS was used to capture the polarization of oxygen anions, that is, a core particle and a satellite shell particle form an oxygen anion and interact by harmonic spring,

$$U_{\mathrm{cs}} = k \cdot r_{\mathrm{cs}}^2. \quad (2)$$

The Coulombic interactions were treated by the particle-particle particle-mesh (pppm) solver[43] and periodic boundary conditions were applied in all directions. We used a cutoff of 9 Å for short-range interactions and 0.2 fs as timestep for all simulations to capture the dynamics of core-shell model. This interaction potential was developed to reproduce the LATP crystalline and amorphous structures, and it shows a more accurate representation of LATP at high temperature, which is needed for melt-

quenching process to produce LATP glass as described below. The detailed parameters for the interaction potential can be found in the Ref.[21]

Glass and glass-ceramic sample preparation. A random structure with stoichiometry of $Li_{1.3}Al_{0.3}Ti_{1.7}(PO_4)_3$ was produced by randomly placing Li_2O, Al_2O, TiO_2, and P_2O_5 units into a box. This structure was melted at 2300 K for 20 ps in *NVT* ensemble and then gradually quenched to 300 K with a cooling rate of 2 K/ps in the *NPT* ensemble. We note that the melted state at 2300 K was confirmed by the mean-squared displacement data shown in **Figure S13c**. The final structure was obtained by equilibration at 300 K for 20 ps in *NPT* and then 20 ps in *NVT* ensembles. The crystalline LATP was obtained by partial substitution of Ti by Al in the LTP crystal, and then it was equilibrated at 300 K for 100 ps. We followed the cut-combine method as described in the Ref[29] to produce LATP glass-ceramics. Specifically, by considering the size, length to diameter ratio, and angle of crystal grain to the pre-crack, as illustrated in **Figure 1d**, we first defined an elliptical crystal region within the large LATP crystalline slab (generated by replicating the unit cell), and deleted the residual atoms. Subsequently, we identified the corresponding elliptical region within a larger melt-quenched LATP glass sample and removed the atoms in that region. The LATP glass-ceramics were constructed by combining the remaining glass matrix with the elliptical crystalline portion. We then annealed the structure near the glass transition temperature (T_g) as shown in **Figure S13b** at 1000 K, resulting in a final configuration with a dimension of ~ 34.08 Å × 486.93 Å × 333.41 Å. We also compared the T_g with the experimentally measured one to ensure that the T_g of simulated LATP glass is within a reasonable range (**Figure S13a**). Different annealing temperatures in the range of 500-1000 K were examined and found to have a negligible impact on the stress-strain curve (**Figure S14**). Furthermore, we found that this low temperature will not heal the interface between the crystal and glass matrix.

***Ab initio* molecular dynamics simulations.** To further validate the accuracy of the LATP structure obtained using classical MD simulations, we also carried out *ab initio* MD simulations (AIMD) to prepare the LATP glass. To this end, we used the Quickstep module[44] of the CP2K package[45] with the hybrid Gaussian[46] and plane wave method (GPW) to simulate the melt-quench process of LATP. To ensure computational efficiency, the basis functions were mapped onto a multi-grid system with the default grid number of 4 with a plane-wave cutoff for the electronic density to be 600 Ry, and a relative cutoff of 40 Ry. The initial structure of LATP crystal was constructed by partial substitution of Ti by Al in the LTP crystal. The system was first equilibrated in the *NVT* ensemble at 300 K for 3.5 ps. The density of the LATP crystal was adapted to the experiment value[37] of 2.69 g cm^{-3} of the glass. The structure was then melted at 4000 K for another 3.5 ps to ensure the loss of the memory of the initial configuration. Subsequently, the system was quenched to the glass state by gradually equilibrated in the *NVT* ensemble at a series of decreasing temperatures with an interval of 400 K for 1 ps (i.e., 3600, 3200, …, and 400 K). The structure analysis of the final glass was based on the trajectory under the equilibration of 300 K for 1.0 ps. The timestep of the simulation was 1.0 fs. The temperature was regulated employing the Nosé–Hoover thermostat.[47] The exchange-correlation energy was computed utilizing the Perdew-Burke-Ernzerhof (PBE) approximation,[48] while dispersion interactions were addressed by incorporating the empirical dispersion correction (D3) developed by Grimme.[49] The pseudopotential GTH-PBE, in conjunction with the corresponding basis sets DZVP-MOLOPT-SR-GTH, was utilized to characterize the behavior of valence electrons.[50]

Structural analysis. The partial radial distribution functions $g_{ij}(r)$ defines the probability of finding a particle j at distance $r + \Delta r$ given that there is a particle i,

$$g_{ij}(r) = \frac{n_{ij}(r)}{4\pi r^2 \mathrm{d}r \rho_j}, \quad (3)$$

where n_{ij} is the number of j-type atoms found in a spherical shell of radius r and thickness Δr, with the centra i-type atom. ρ_j is the number density of j-type atoms. The coordination $n(r)$ is obtained by intergrating $g_{ij}(r)$ between r_1 and r_2 as,

$$\mathrm{n}\,(r) = \int_{r_1}^{r_2} 4\pi r^2 \rho_j g_{ij}(r) \mathrm{d}r. \quad (4)$$

The local coordination numbers are measured from $n(r)$ at the cut-off of 2.25 Å (the first minimum of $g_{\mathrm{Al\text{-}O}}(r)$ and $g_{\mathrm{Ti\text{-}O}}(r)$) for Al-O and Ti-O pairs.

Fracture simulations. The fracture behavior of LATP electrolytes is analyzed by applying tensile loading. We followed the method developed by Brochard et al.[51] In detail, an ellipse shape pre-crack (a = 60.2 Å, b = 13.5 Å) was introduced by removing the atoms in the center of the simulated structure. Then the system was equilibrated in *NPT* ensemble at 300 K and subsequently applied a uniaxial tensile loading until full fracture; this was achieved by elongating the structure along the y direction with a fixed strain rate of 5×10^9 s^{-1} for all fracture simulation. Through a comparative analysis of fracture simulations conducted at three distinct strain rates of 1, 5, and 10×10^9 s^{-1}, we observe a distinct alteration in the stress-strain profiles. An increase in strain rate corresponds to an increase in the cumulative area encompassed by the stress-strain curves as depicted in **Figures S15a** and **S15b** for LATP-GC3 and LATP-GC15 samples, respectively. However, importantly, the trend remains the same for all three strain rates and also considering the computational costs, we opted for a strain rate of 5×10^{-9} s^{-1} for the fracture simulations.

Based on the recorded strain-stress curve, Young's modulus E was calculated from its slope in the low strain region (strain below 0.01). The fracture energy G_c was calculated by integrating the stress-strain curve.[52]

$$G_{\mathrm{c}} = \frac{L_x L_y L_z}{\Delta A} \int_0^{\varepsilon_{yy}^{\mathrm{f}}} \sigma_{yy} \mathrm{d}\varepsilon_{yy}, \quad (5)$$

where L is the length of the simulation box, ΔA is the crack surface area generated by fracture, and ε^{f} corresponds to the fully fractured strain.

Bond switching analysis. The rearrangement of atoms during fracture process results in the breaking and re-forming of bonds. We counted these so-called bond switching events[31] of atomic coordination number (CN) changes during fracture simulations. To this end, we first calculated the partial RDFs, as shown in **Figure 2** and **Figure S1**. The atoms i and j are considered bonded within the distance based on the first minimum of $g_{ij}(r)$, which is 2.25 Å for the Al-O and Ti-O in our study. By analyzing the CN and nearest-neighboring atom ID and comparing to the non-strained structure, the bond switching evens can be classified into decreased and increased CN if the coordination is changed, while we count it as swapped if the CN is the same as in the initial structure. The unchanged CN is the faction of the atoms that do not exhibit bond switching events. Due to the higher lithium mobility, we did not count the bond switching events of Li-O.

Conflicts of interest
There are no conflicts to declare.

Acknowledgements
This work was supported by grants from the China Scholarship Council (202106880010), Marie Skłodowska-Curie Individual Fellowship (101018156), and Independent Research Fund Denmark (1127-00003). We also acknowledge the computational resources supplied by Danish e-infrastructure Cooperation (DeiC) National HPC (DeiC-AAU-N5-202200005), and EuroHPC Joint Undertaking with access to Vega at IZUM, Slovenia (EHPC-REG-2022R02-224).

References
(1) Armand, M.; Tarascon, J.-M. Building Better Batteries. *Nature* **2008**, *451* (7179), 652–657. https://doi.org/10.1038/451652a.
(2) Pang, Q.; Meng, J.; Gupta, S.; Hong, X.; Kwok, C. Y.; Zhao, J.; Jin, Y.; Xu, L.; Karahan, O.; Wang, Z.; Toll, S.; Mai, L.; Nazar, L. F.; Balasubramanian, M.; Narayanan, B.; Sadoway, D. R. Fast-Charging Aluminium–Chalcogen Batteries Resistant to Dendritic Shorting. *Nature* **2022**, *608* (7924), 704–711. https://doi.org/10.1038/s41586-022-04983-9.
(3) Goodenough, J. B.; Park, K.-S. The Li-Ion Rechargeable Battery: A Perspective. *J. Am. Chem. Soc.* **2013**, *135* (4), 1167–1176. https://doi.org/10.1021/ja3091438.
(4) Kato, Y.; Hori, S.; Saito, T.; Suzuki, K.; Hirayama, M.; Mitsui, A.; Yonemura, M.; Iba, H.; Kanno, R. High-Power All-Solid-State Batteries Using Sulfide Superionic Conductors. *Nat. Energy* **2016**, *1* (4), 16030. https://doi.org/10.1038/nenergy.2016.30.
(5) Janek, J.; Zeier, W. G. A Solid Future for Battery Development. *Nat. Energy* **2016**, *1* (9), 16141. https://doi.org/10.1038/nenergy.2016.141.
(6) Famprikis, T.; Canepa, P.; Dawson, J. A.; Islam, M. S.; Masquelier, C. Fundamentals of Inorganic Solid-State Electrolytes for Batteries. *Nat. Mater.* **2019**, *18* (12), 1278–1291. https://doi.org/10.1038/s41563-019-0431-3.
(7) Shen, C.; Huang, Y.; Yang, J.; Chen, M.; Liu, Z. Unraveling the Mechanism of Ion and Electron Migration in Composite Solid-State Electrolyte Using Conductive Atomic Force Microscopy. *Energy Storage Mater.* **2021**, *39*, 271–277. https://doi.org/10.1016/j.ensm.2021.04.028.
(8) Wan, H.; Wang, Z.; Liu, S.; Zhang, B.; He, X.; Zhang, W.; Wang, C. Critical Interphase Overpotential as a Lithium Dendrite-Suppression Criterion for All-Solid-State Lithium Battery Design. *Nat. Energy* **2023**, 1–9. https://doi.org/10.1038/s41560-023-01231-w.
(9) Zhang, Z.; Shao, Y.; Lotsch, B.; Hu, Y.-S.; Li, H.; Janek, J.; Nazar, L. F.; Nan, C.-W.; Maier, J.; Armand, M.; Chen, L. New Horizons for Inorganic Solid State Ion Conductors. *Energy Environ. Sci.* **2018**, *11* (8), 1945–1976. https://doi.org/10.1039/C8EE01053F.
(10) Zheng, Y.; Yao, Y.; Ou, J.; Li, M.; Luo, D.; Dou, H.; Li, Z.; Amine, K.; Yu, A.; Chen, Z. A Review of Composite Solid-State Electrolytes for Lithium Batteries: Fundamentals, Key Materials and Advanced Structures. *Chem. Soc. Rev.* **2020**, *49* (23), 8790–8839. https://doi.org/10.1039/D0CS00305K.
(11) Xiao, W.; Wang, J.; Fan, L.; Zhang, J.; Li, X. Recent Advances in $Li_{1+x}Al_xTi_{2-x}(PO_4)_3$ Solid-

State Electrolyte for Safe Lithium Batteries. *Energy Storage Mater.* **2019**, *19*, 379–400. https://doi.org/10.1016/j.ensm.2018.10.012.
(12) Yang, K.; Chen, L.; Ma, J.; He, Y.; Kang, F. Progress and Perspective of $Li_{1+x}Al_xTi_{2-x}(PO_4)_3$ Ceramic Electrolyte in Lithium Batteries. *InfoMat* **2021**, *3* (11), 1195–1217. https://doi.org/10.1002/inf2.12222.
(13) McConohy, G.; Xu, X.; Cui, T.; Barks, E.; Wang, S.; Kaeli, E.; Melamed, C.; Gu, X. W.; Chueh, W. C. Mechanical Regulation of Lithium Intrusion Probability in Garnet Solid Electrolytes. *Nat. Energy* **2023**, 1–10. https://doi.org/10.1038/s41560-022-01186-4.
(14) Tippens, J.; Miers, J. C.; Afshar, A.; Lewis, J. A.; Cortes, F. J. Q.; Qiao, H.; Marchese, T. S.; Di Leo, C. V.; Saldana, C.; McDowell, M. T. Visualizing Chemomechanical Degradation of a Solid-State Battery Electrolyte. *ACS Energy Lett.* **2019**, *4* (6), 1475–1483. https://doi.org/10.1021/acsenergylett.9b00816.
(15) Mangani, L. R.; Villevieille, C. Mechanical *vs.* Chemical Stability of Sulphide-Based Solid-State Batteries. Which One Is the Biggest Challenge to Tackle? Overview of Solid-State Batteries and Hybrid Solid State Batteries. *J. Mater. Chem. A* **2020**, *8* (20), 10150–10167. https://doi.org/10.1039/D0TA02984J.
(16) Garcia-Mendez, R.; Smith, J. G.; Neuefeind, J. C.; Siegel, D. J.; Sakamoto, J. Correlating Macro and Atomic Structure with Elastic Properties and Ionic Transport of Glassy Li_2S-P_2S_5 (LPS) Solid Electrolyte for Solid-State Li Metal Batteries. *Adv. Energy Mater.* **2020**, *10* (19), 2000335. https://doi.org/10.1002/aenm.202000335.
(17) Hikima, K.; Totani, M.; Obokata, S.; Muto, H.; Matsuda, A. Mechanical Properties of Sulfide-Type Solid Electrolytes Analyzed by Indentation Methods. *ACS Appl. Energy Mater.* **2022**, *5* (2), 2349–2355. https://doi.org/10.1021/acsaem.1c03829.
(18) Yoon, I.; Jurng, S.; Abraham, D. P.; Lucht, B. L.; Guduru, P. R. Measurement of Mechanical and Fracture Properties of Solid Electrolyte Interphase on Lithium Metal Anodes in Lithium Ion Batteries. *Energy Storage Mater.* **2020**, *25*, 296–304. https://doi.org/10.1016/j.ensm.2019.10.009.
(19) Luo, J. Interfacial Engineering of Solid Electrolytes. *J. Materiomics* **2015**, *1* (1), 22–32. https://doi.org/10.1016/j.jmat.2015.03.002.
(20) Cantwell, P. R.; Frolov, T.; Rupert, T. J.; Krause, A. R.; Marvel, C. J.; Rohrer, G. S.; Rickman, J. M.; Harmer, M. P. Grain Boundary Complexion Transitions. *Annu. Rev. Mater. Res.* **2020**, *50* (1), 465–492. https://doi.org/10.1146/annurev-matsci-081619-114055.
(21) Stegmaier, S.; Schierholz, R.; Povstugar, I.; Barthel, J.; Rittmeyer, S. P.; Yu, S.; Wengert, S.; Rostami, S.; Kungl, H.; Reuter, K.; Eichel, R.; Scheurer, C. Nano-Scale Complexions Facilitate Li Dendrite-Free Operation in LATP Solid-State Electrolyte. *Adv. Energy Mater.* **2021**, *11* (26), 2100707. https://doi.org/10.1002/aenm.202100707.
(22) Duan, S.; Yu, J.; Sun, Y.; Li, A.; Chen, S.; Qu, K.; Ding, Z.; Liu, Z.; Li, Y.; Huang, C.; Liu, M.; Liu, J.; Shi, J.; Huang, B.; Tian, X.; Hou, S.; Xie, S.; Liu, Y.; Gao, P.; Li, J.; Jin, H. Selective Doping to Relax Glassified Grain Boundaries Substantially Enhances the Ionic Conductivity of $LiTi_2(PO_4)_3$ Glass-Ceramic Electrolytes. *J. Power Sources* **2020**, *449*, 227574. https://doi.org/10.1016/j.jpowsour.2019.227574.
(23) Davis, C.; Nino, J. C. Microwave Processing for Improved Ionic Conductivity in Li_2O–Al_2O_3–TiO_2–P_2O_5 Glass-Ceramics. *J. Am. Ceram. Soc.* **2015**, *98* (8), 2422–2427. https://doi.org/10.1111/jace.13638.

(24) Aono, H.; Sugimoto, E.; Sadaoka, Y.; Imanaka, N.; Adachi, G. Ionic Conductivity of Solid Electrolytes Based on Lithium Titanium Phosphate. *J. Electrochem. Soc.* **1990**, *137* (4), 1023. https://doi.org/10.1149/1.2086597.
(25) Duluard, S.; Paillassa, A.; Puech, L.; Vinatier, P.; Turq, V.; Rozier, P.; Lenormand, P.; Taberna, P.-L.; Simon, P.; Ansart, F. Lithium Conducting Solid Electrolyte $Li_{1.3}Al_{0.3}Ti_{1.7}(PO_4)_3$ Obtained via Solution Chemistry. *J. Eur. Ceram. Soc.* **2013**, *33* (6), 1145–1153. https://doi.org/10.1016/j.jeurceramsoc.2012.08.005.
(26) Tezuka, T.; Kuribara, K.; Kodama, S.; Takeda, H.; Yanase, I. Synthesis and Ionic Conductivity of NASICON-Type $Li_{1.4}Al_{0.4}Ti_{1.6}(PO_4)_3$ Fine Powder by a Novel Multi-Step Glass Crystallization Method. *J. Non-Cryst. Solids* **2022**, *590*, 121675. https://doi.org/10.1016/j.jnoncrysol.2022.121675.
(27) DeWees, R.; Wang, H. Synthesis and Properties of NaSICON-type LATP and LAGP Solid Electrolytes. *ChemSusChem* **2019**, *12* (16), 3713–3725. https://doi.org/10.1002/cssc.201900725.
(28) Kyung Shin, Y.; Y. Sengul, M.; M. Jonayat, A. S.; Lee, W.; D. Gomez, E.; A. Randall, C.; van Duin, A. C. T. Development of a ReaxFF Reactive Force Field for Lithium Ion Conducting Solid Electrolyte $Li_{1+x}Al_xTi_{2-x}(PO_4)_3$ (LATP). *Phys. Chem. Chem. Phys.* **2018**, *20* (34), 22134–22147. https://doi.org/10.1039/C8CP03586E.
(29) Deng, B.; Harris, J. T. A Novel Approach to Generate Glass-Ceramics Samples for Molecular Dynamics Simulations. *Comput. Mater. Sci.* **2021**, *186*, 110008. https://doi.org/10.1016/j.commatsci.2020.110008.
(30) Deng, B.; Luo, J.; Harris, J. T.; Smith, C. M.; Wilkinson, T. M. Toward Revealing Full Atomic Picture of Nanoindentation Deformation Mechanisms in Li_2O-$2SiO_2$ Glass-Ceramics. *Acta Mater.* **2021**, *208*, 116715. https://doi.org/10.1016/j.actamat.2021.116715.
(31) Frankberg, E. J.; Kalikka, J.; García Ferré, F.; Joly-Pottuz, L.; Salminen, T.; Hintikka, J.; Hokka, M.; Koneti, S.; Douillard, T.; Le Saint, B.; Kreiml, P.; Cordill, M. J.; Epicier, T.; Stauffer, D.; Vanazzi, M.; Roiban, L.; Akola, J.; Di Fonzo, F.; Levänen, E.; Masenelli-Varlot, K. Highly Ductile Amorphous Oxide at Room Temperature and High Strain Rate. *Science* **2019**, *366* (6467), 864–869. https://doi.org/10.1126/science.aav1254.
(32) To, T.; Sørensen, S. S.; Christensen, J. F. S.; Christensen, R.; Jensen, L. R.; Bockowski, M.; Bauchy, M.; Smedskjaer, M. M. Bond Switching in Densified Oxide Glass Enables Record-High Fracture Toughness. *ACS Appl. Mater. Interfaces* **2021**, *13* (15), 17753–17765. https://doi.org/10.1021/acsami.1c00435.
(33) Du, T.; Liu, H.; Tang, L.; Sørensen, S. S.; Bauchy, M.; Smedskjaer, M. M. Predicting Fracture Propensity in Amorphous Alumina from Its Static Structure Using Machine Learning. *ACS Nano* **2021**, *15* (11), 17705–17716. https://doi.org/10.1021/acsnano.1c05619.
(34) Redhammer, G. J.; Rettenwander, D.; Pristat, S.; Dashjav, E.; Kumar, C. M. N.; Topa, D.; Tietz, F. A Single Crystal X-Ray and Powder Neutron Diffraction Study on NASICON-Type $Li_{1+x}Al_xTi_{2-x}(PO_4)_3$ ($0 \leq x \leq 0.5$) Crystals: Implications on Ionic Conductivity. *Solid State Sci.* **2016**, *60*, 99–107. https://doi.org/10.1016/j.solidstatesciences.2016.08.011.
(35) Lang, B.; Ziebarth, B.; Elsässer, C. Lithium Ion Conduction in $LiTi_2(PO_4)_3$ and Related Compounds Based on the NASICON Structure: A First-Principles Study. *Chem. Mater.* **2015**, *27* (14), 5040–5048. https://doi.org/10.1021/acs.chemmater.5b01582.
(36) Waetzig, K.; Rost, A.; Langklotz, U.; Matthey, B.; Schilm, J. An Explanation of the Microcrack Formation in $Li_{1.3}Al_{0.3}Ti_{1.7}(PO_4)_3$ Ceramics. *J. Eur. Ceram. Soc.* **2016**, *36* (8), 1995–

2001. https://doi.org/10.1016/j.jeurceramsoc.2016.02.042.
(37) Thokchom, J.; Kumar, B. Microstructural Effects on the Superionic Conductivity of a Lithiated Glass-Ceramic. *Solid State Ion.* **2006**, *177* (7–8), 727–732. https://doi.org/10.1016/j.ssi.2006.01.027.
(38) Zhu, J.; Zhao, J.; Xiang, Y.; Lin, M.; Wang, H.; Zheng, B.; He, H.; Wu, Q.; Huang, J. Y.; Yang, Y. Chemomechanical Failure Mechanism Study in NASICON-Type $Li_{1.3}Al_{0.3}Ti_{1.7}(PO_4)_3$ Solid-State Lithium Batteries. *Chem. Mater.* **2020**, *32* (12), 4998–5008. https://doi.org/10.1021/acs.chemmater.9b05295.
(39) Deng, Z.; Wang, Z.; Chu, I.-H.; Luo, J.; Ong, S. P. Elastic Properties of Alkali Superionic Conductor Electrolytes from First Principles Calculations. *J. Electrochem. Soc.* **2015**, *163* (2), A67. https://doi.org/10.1149/2.0061602jes.
(40) Yan, G.; Yu, S.; Yang, W.; Li, X.; Tempel, H.; Kungl, H.; Eichel, R.-A.; Krüger, M.; Malzbender, J. Anisotropy of the Mechanical Properties of $Li_{1.3}Al_{0.3}Ti_{1.7}(PO_4)_3$ Solid Electrolyte Material. *J. Power Sources* **2019**, *437*, 226940. https://doi.org/10.1016/j.jpowsour.2019.226940.
(41) Plimpton, S. Fast Parallel Algorithms for Short-Range Molecular Dynamics. *J. Comput. Phys.* **1995**, *117* (1), 1–19. https://doi.org/10.1006/jcph.1995.1039.
(42) Stukowski, A. Visualization and Analysis of Atomistic Simulation Data with OVITO–the Open Visualization Tool. *Model. Simul. Mater. Sci. Eng.* **2009**, *18* (1), 015012. https://doi.org/10.1088/0965-0393/18/1/015012.
(43) Eastwood, R. W. H., J. W. *Computer Simulation Using Particles*; CRC Press: Boca Raton, 2021. https://doi.org/10.1201/9780367806934.
(44) VandeVondele, J.; Krack, M.; Mohamed, F.; Parrinello, M.; Chassaing, T.; Hutter, J. Quickstep: Fast and Accurate Density Functional Calculations Using a Mixed Gaussian and Plane Waves Approach. *Comput. Phys. Commun.* **2005**, *167* (2), 103–128. https://doi.org/10.1016/j.cpc.2004.12.014.
(45) Kühne, T. D.; Iannuzzi, M.; Del Ben, M.; Rybkin, V. V.; Seewald, P.; Stein, F.; Laino, T.; Khaliullin, R. Z.; Schütt, O.; Schiffmann, F.; Golze, D.; Wilhelm, J.; Chulkov, S.; Bani-Hashemian, M. H.; Weber, V.; Borštnik, U.; Taillefumier, M.; Jakobovits, A. S.; Lazzaro, A.; Pabst, H.; Müller, T.; Schade, R.; Guidon, M.; Andermatt, S.; Holmberg, N.; Schenter, G. K.; Hehn, A.; Bussy, A.; Belleflamme, F.; Tabacchi, G.; Glöß, A.; Lass, M.; Bethune, I.; Mundy, C. J.; Plessl, C.; Watkins, M.; VandeVondele, J.; Krack, M.; Hutter, J. CP2K: An Electronic Structure and Molecular Dynamics Software Package - Quickstep: Efficient and Accurate Electronic Structure Calculations. *J. Chem. Phys.* **2020**, *152* (19), 194103. https://doi.org/10.1063/5.0007045.
(46) Kohn, W.; Sham, L. J. Self-Consistent Equations Including Exchange and Correlation Effects. *Phys. Rev.* **1965**, *140* (4A), A1133–A1138. https://doi.org/10.1103/PhysRev.140.A1133.
(47) Nosé, S. A Molecular Dynamics Method for Simulations in the Canonical Ensemble. *Mol. Phys.* **1984**, *52* (2), 255–268. https://doi.org/10.1080/00268978400101201.
(48) Perdew, J. P.; Burke, K.; Ernzerhof, M. Generalized Gradient Approximation Made Simple. *Phys. Rev. Lett.* **1996**, *77* (18), 3865–3868. https://doi.org/10.1103/PhysRevLett.77.3865.
(49) Grimme, S.; Antony, J.; Ehrlich, S.; Krieg, H. A Consistent and Accurate Ab Initio Parametrization of Density Functional Dispersion Correction (DFT-D) for the 94 Elements H-Pu. *J. Chem. Phys.* **2010**, *132* (15), 154104. https://doi.org/10.1063/1.3382344.
(50) Goedecker, S.; Teter, M.; Hutter, J. Separable Dual-Space Gaussian Pseudopotentials. *Phys.*

Rev. B **1996**, *54* (3), 1703–1710. https://doi.org/10.1103/PhysRevB.54.1703.
(51) Brochard, L.; Hantal, G.; Laubie, H.; Ulm, F. J.; Pellenq, R. J.-M. Fracture Mechanisms in Organic-Rich Shales: Role of Kerogen. *Poromechanics V Proc. Fifth Biot Conf. Poromechanics* **2013**, 2471–2480. https://doi.org/10.1061/9780784412992.288.
(52) Ravinder, R.; Kumar, A.; Kumar, R.; Vangla, P.; Krishnan, N. M. A. Irradiation-Induced Brittle-to-Ductile Transition in α-Quartz. *J. Am. Ceram. Soc.* **2020**, *103* (7), 3962–3970. https://doi.org/10.1111/jace.16951.